Title

Shape-based motion correction in dynamic contrast-enhanced MRI for quantitative assessment of renal function

Journal

Medical Physics, 41(12)

ISSN

0094-2405

Authors

Liu, Wenyang
Sung, Kyunghyun
Ruan, Dan

Publication Date

2014-11-18

DOI

10.1118/1.4900600

Peer reviewed

Medical Physics
The International Journal of Medical Physics Research and Practice

Shape-based motion correction in dynamic contrast-enhanced MRI for quantitative assessment of renal function

Wenyang Liu, Kyunghyun Sung, and Dan Ruan

Citation: Medical Physics **41**, 122302 (2014); doi: 10.1118/1.4900600
View online: http://dx.doi.org/10.1118/1.4900600
View Table of Contents: http://scitation.aip.org/content/aapm/journal/medphys/41/12?ver=pdfcov
Published by the American Association of Physicists in Medicine

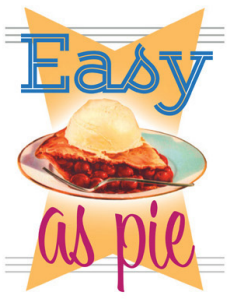

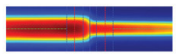

Shape-based motion correction in dynamic contrast-enhanced MRI for quantitative assessment of renal function

Wenyang Liu
Department of Bioengineering, University of California, Los Angeles 90095

Kyunghyun Sung
Department of Bioengineering, University of California, Los Angeles 90095 and Department of Radiological Sciences, University of California, Los Angeles 90095

Dan Ruan[a)]
Department of Bioengineering, University of California, Los Angeles 90095 and Department of Radiation Oncology, University of California, Los Angeles 90095

(Received 19 June 2014; revised 12 September 2014; accepted for publication 11 October 2014; published 18 November 2014)

Purpose: To incorporate a newly developed shape-based motion estimation scheme into magnetic resonance urography (MRU) and verify its efficacy in facilitating quantitative functional analysis.
Methods: The authors propose a motion compensation scheme in MRU that consists of three sequential modules: MRU image acquisition, motion compensation, and quantitative functional analysis. They designed two sets of complementary experiments to evaluate the performance of the proposed method. In the first experiment, dynamic contrast enhanced (DCE) MR images were acquired from three sedated subjects, from which clinically valid estimates were derived and served as the "ground truth." Physiologically sound motion was then simulated to synthesize image sequences influenced by respiratory motion. Quantitative assessment and comparison were performed on functional estimates of Patlak number, glomerular filtration rate, and Patlak differential renal function without and with motion compensation against the ground truth. In the second experiment, the authors acquired a temporal series of noncontrast MR images under free breathing from a healthy adult subject. The performance of the proposed method on compensating real motion was evaluated by comparing the standard deviation of the obtained temporal intensity curves before and after motion compensation.
Results: On DCE-MR images with simulated motion, the generated relative enhancement curves exhibited large perturbations and the Patlak numbers of the left and right kidney were significantly underestimated up to 35% and 34%, respectively, compared with the ground truth. After motion compensation, the relative enhancement curves exhibited much less perturbations and Patlak estimation errors reduced within 3% and 4% for the left and right kidneys, respectively. On clinical free-breathing MR images, the temporal intensity curves exhibited significantly reduced variations after motion compensation, with standard deviation decreased from 30.3 and 38.2 to 8.3 and 11.7 within two manually selected regions of interest, respectively.
Conclusions: The developed motion compensation method has demonstrated its ability to facilitate quantitative MRU functional analysis, with improved accuracy of pharmacokinetic modeling and quantitative parameter estimations. Future work will consider performing more intensive clinical verifications with sophisticated pharmacokinetic models and generalizing the proposed method to other quantitative DCE analysis, such as on liver or prostate function. [http://dx.doi.org/10.1118/1.4900600]

Key words: DCE-MRI, motion correction, kidney, quantitative analysis

1. INTRODUCTION

Dynamic contrast-enhanced magnetic resonance imaging (DCE-MRI) is a widely used technique and a promising radiological measure of renal function.[1] In particular, magnetic resonance urography (MRU) provides both morphological information and quantitative functional evaluations of the urinary tract in a single examination[2,3] and offers high contrast and superior resolution compared with conventional techniques.[4] Free of radiation, MRU has been widely used in pediatric subjects. During MRU, images are usually acquired before, during, and after the injection of the contrast agent (such as Gd-DTPA) to capture the dynamic signals. These dynamic signal changes reflect the perfusion, filtration, concentration, and excretion of the kidney, and one can analyze the MRU data to obtain quantitative functional information such as renal transit time (RTT), glomerular filtration rate (GFR), differential renal function (DRF), and relative time–signal intensity.[3]

Motion artifacts can cause substantial errors in estimating quantitative parameters.[5,6] In most MRU studies, motion artifacts are minimized by scanning subjects under sedation, gating, or taking sequential breath-holds.[2] However, those techniques are not desirable in that sedation often requires

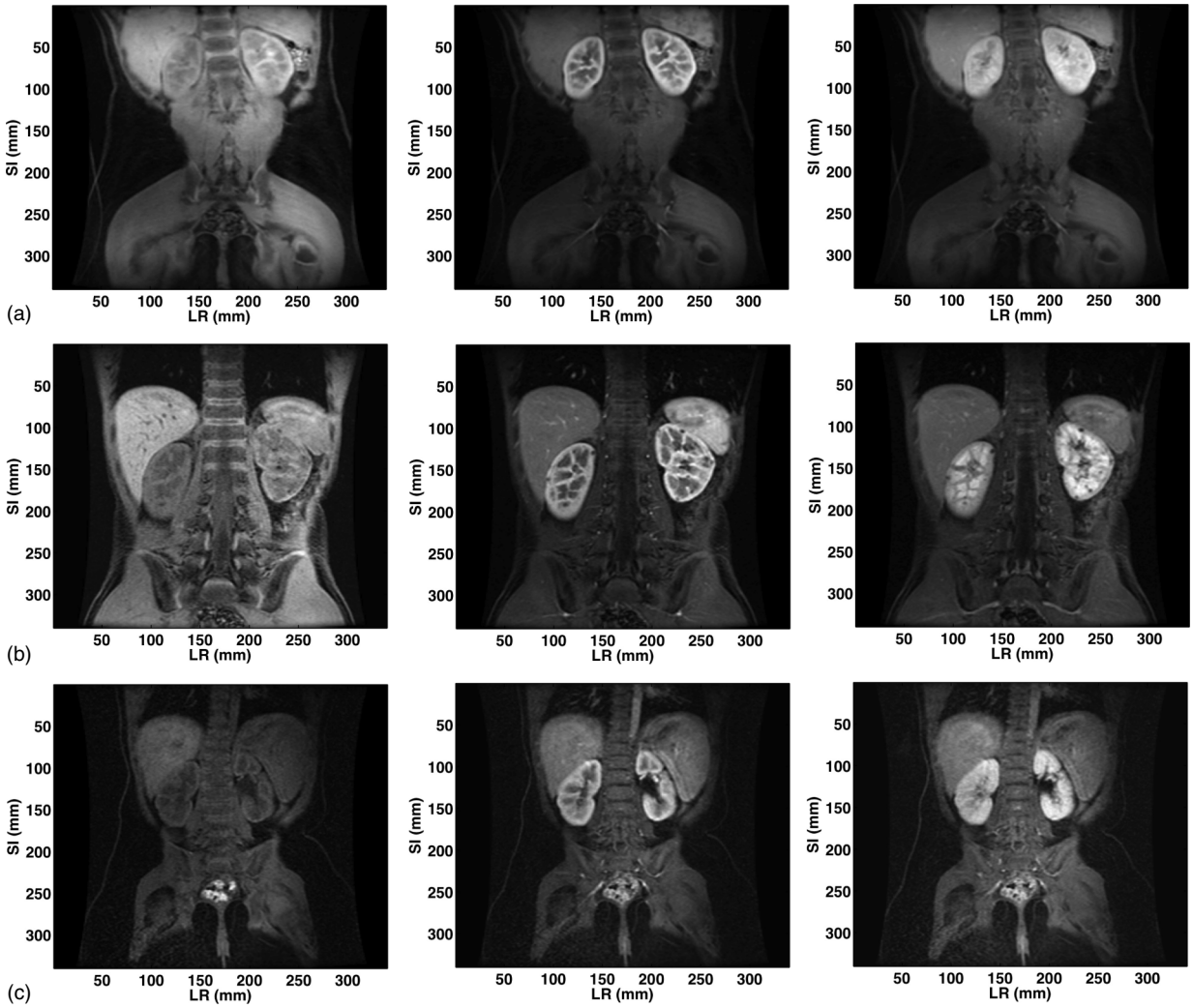

FIG. 1. Example images for three subjects with different enhancement stages after contrast agent injection at 0, 72, and 180 s, respectively.

dedicated sedation physicians to titrate dose for each subject, gating scarifies efficiency and temporal resolution, and breath-holding requires patient cooperation that could be challenging for pediatric patients. Recently, efforts have been made to perform motion compensation by post image processing.[7–9] However, contrast changes due to the pharmacokinetics make the motion compensation challenging.

Recent approaches have been proposed by applying matching metrics that are insensitive to contrast changes. One approach is to consider the contrast-variant images as effectively different modalities and to maximize the mutual information.[9] However, the locally changing pattern in DCE-MR images does not guarantee the assumed mapping consistency and may lead to large registration errors.[10,11] Similarly, the cross-correlation metric proposed in Ref. 8 may also be violated in DCE-MR images.

Recently, we have developed a novel methodology to perform nonrigid motion estimation based on geometrical features that are robust to intensity and contrast variations—an approach particularly applicable in DCE-MRI motion correction.[12] In this study, we propose to incorporate this motion correction method into the MRU functional analysis framework and validate this framework directly with clinical endpoints in quantitative MRU analysis—the Patlak number, GFR, and DRF. Specifically, we designed two complementary experiments to assess its performance. In the first experiment centered on quantitative validation, we obtained the clinically valid functional estimates from DCE-MR images acquired under sedation as the "ground truth" and quantitatively compared the obtained functional estimates from the proposed method on the simulated motion-affected DCE-MR images against the ground truth. To faithfully capture and reflect the involved motion impact on MR imaging, a second set of experiment was conducted on MR images acquired under free-breathing without contrast enhancement, and the performance was evaluated by assessing the temporal variation of intensity curves within various regions of interest (ROIs).

2. MATERIALS AND METHODS

2.A. MR image acquisition

The imaging protocols used in this study were approved by the local institutional review board. Each enrolled subject

was screened for MRI risk factors and provided informed consent in accordance with institutional policy.

2.A.1. DCE-MR image acquisition with triggering and sedation

The DCE-MR images in this study were acquired on a 3.0T GE MR 750 system (GE Healthcare, Waukesha, WI) with subjects under general anesthesia, where the ground truth functional estimates can be obtained. Bellows respiratory triggering was implemented resulting in a temporal phase every two respiratory cycles (temporal resolution is about 9 s/dynamic volume for a 20 cycles/min respiratory rate). To ensure general applicability, we have carefully chosen three pediatric patients (17 month, 6 yr, and 9 yr old, respectively) that have significant variations of anatomical characterizations and enhancement behaviors. To achieve better linearity between MRI signal and contrast concentration and to avoid potential kidney problems, a low dose at 1/5 of Gadovist (Gd-DO3A-butriol, Schering AG, Berlin) was used as the contrast agent with the injection rate of 0.3 mL/s, followed by 10 mL saline chaser at the same rate. A body coil was used for RF transmission, and a commercially available 32-channel torso array coil was used with the anterior 19 elements enabled for the data acquisition. Parallel imaging was used with an acceleration factor of 2×2. A 3D T1-weighted gradient echo sequence with a dual-echo bipolar readout was used for data acquisition, and we used an in-house variable density Cartesian undersampling scheme called DISCO (differential subsampling with cartesian ordering)[13] to perform high spatiotemporal resolution dynamic MRU. A two-point Dixon reconstruction was used for robust fat–water separation. 4D datasets with 47, 34, and 29 temporal volumetric images were acquired for each subject. Imaging parameters were: flip angle = 15°, receiver bandwidth = ±167 kHz, TR = 3.56 ms, matrix size = 256×256, FOV = 340×340 mm^2, the total number of slices = 34, and slice thickness = 4 mm. Figure 1 shows example images from different contrast stages for the three subjects.

2.A.2. Noncontrast MR image acquisition under free breathing

The noncontrast MR images in this study were acquired on a 3.0T MRI system (Skyra, Siemens Healthcare, Erlangen, Germany) from a healthy 27-yr-old male subject. A spline and body matrix coil was used. A similar 3D T1-weighted gradient echo sequence with a dual-echo bipolar readout was used for data acquisition (a TWIST-Dixon work-in-progress sequence[14]) to achieve high spatiotemporal resolution, and the same two-point Dixon reconstruction was used for robust fat–water separation. No parallel imaging was used in this acquisition. The 4D noncontrast MRI dataset contains 12 volumetric images. The imaging parameters were: flip angle = 12°, TR = 4.1 ms, matrix size = 160×152, FOV = 350×350 mm^2, the total number of slices = 28, and slice thickness = 3.1 mm. Figure 2 shows example free-breathing images at different time points, with dominant motion in the superior–inferior (SI) direction and mean magnitude about 14 mm.

2.B. MRU functional analysis

In this study, we focus the quantitative analysis on the following three MRU functional estimations: relative intensity versus time curves, Patlak number of each kidney, and Patlak differential renal function (pDRF).

2.B.1. Relative enhancement curves

The relative enhancement curves are used for comparing two renal functions.[15] The delay of the corticomedullary crossover point, defined as the point where the cortex curve intersects with the medulla curve, is usually used to determine the urinary obstruction.[3,16] A common approach is to manually segment the renal cortex, medulla, and aorta to acquire the enhancement curves of each regions, respectively, and then perform the comparison.[15,17] In each region, a mean signal $S_R(t)$ is calculated at each time point and the relative enhancement curves are calculated by

$$S_R(t) = \frac{S_{R,t} - S_{R,0}}{S_{R,0}}, \tag{1}$$

where R is the region index, $S_{R,t}$ represents the mean signal intensity at time point t for region R, and $S_{R,0}$ is the mean precontrast signal calculated from the baseline scans for region R.

2.B.2. Patlak number

The Patlak number, usually serving as the GFR index of each kidney, can be estimated by the Patlak–Rutland

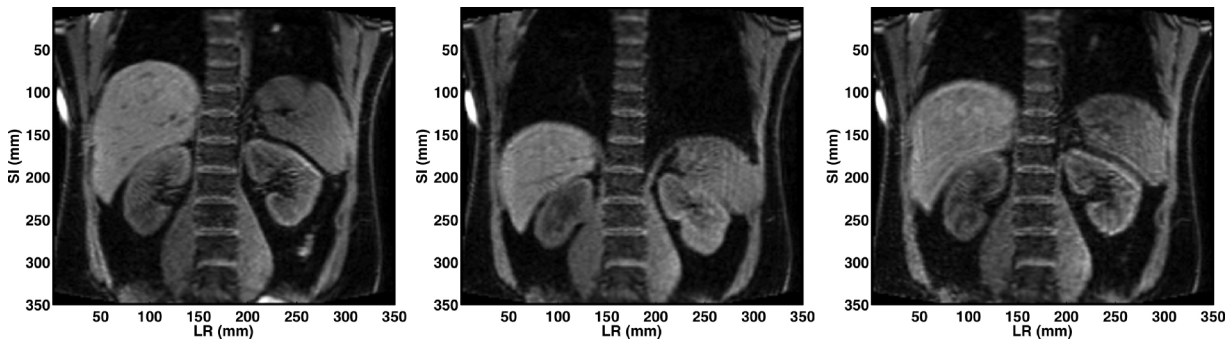

FIG. 2. Example images of the subject under free breathing at 9.7, 14.9, and 35.7 s, respectively.

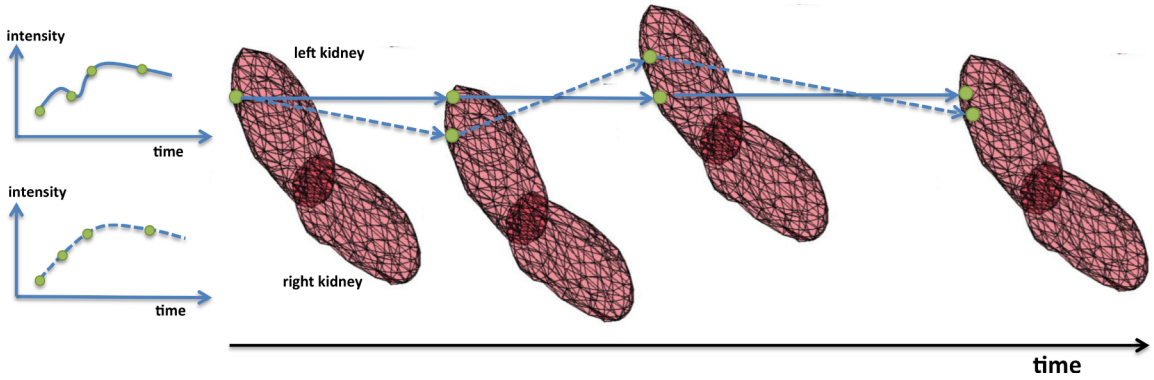

FIG. 3. Illustration of the proposed motion correction scheme: the proposed method is capable of finding the corresponding points in time (tracking voxel trajectory along the dashed line), compared to a "blind" approach where intensity values at the same spatial physical coordinate instead of intrinsic anatomical/functional coordinate are plotted (solid line).

model.[18–20] It is based on a simplified two-compartment model with the following assumptions: the plasma concentration of the contrast agent in the aorta and renal arteries is equal and is proportional to the signal change; the total contrast in the kidney at any time point can be expressed as the sum of the contrast in the vascular space and in the nephrons; the contrast agent does not leave the renal parenchyma during the time of analysis. The amount of contrast agent at any time point $K(t)$ is described as

$$K(t) = V_0 c_a(t) + P \int_0^t c_a(u)du, \tag{2}$$

where V_0 represents the kidney vascular volume, P is the clearance function of the contrast agents from the vascular space to the kidney, and c_a represents the agent concentration in plasma. $K(t)$ can also be represented by $c_k(t)V_k$, where $c_k(t)$ is the mean concentration of contrast agent in the kidney and V_k is the renal volume. Equation (2) can therefore be written as

$$\frac{c_k(t)}{c_a(t)} = \frac{V_0}{V_k} + P\frac{\int_0^t c_a(u)du}{V_k c_a(t)}. \tag{3}$$

At time points before contrast agents excrete into the collecting system, the above equation can be fitted into one linear equation. By assuming that the relative signals and the concentration of contrast agent has a linear relationship, one can replace $c_a(t)$ and $c_k(t)$ by the relative signal calculated from aorta ($S_a(t)$) and renal cortex ($S_c(t)$). The slope P (the Patlak number), representing the clearance rate of contrast agents from the vasculature, can then be estimated by regressing $S_c(t)/S_a(t)$ against $\int_0^t S_a(u)du/V_k S_a(t)$. A convention measurement of GFR can also be obtained by multiplying the Patlak number with the renal volume.[21]

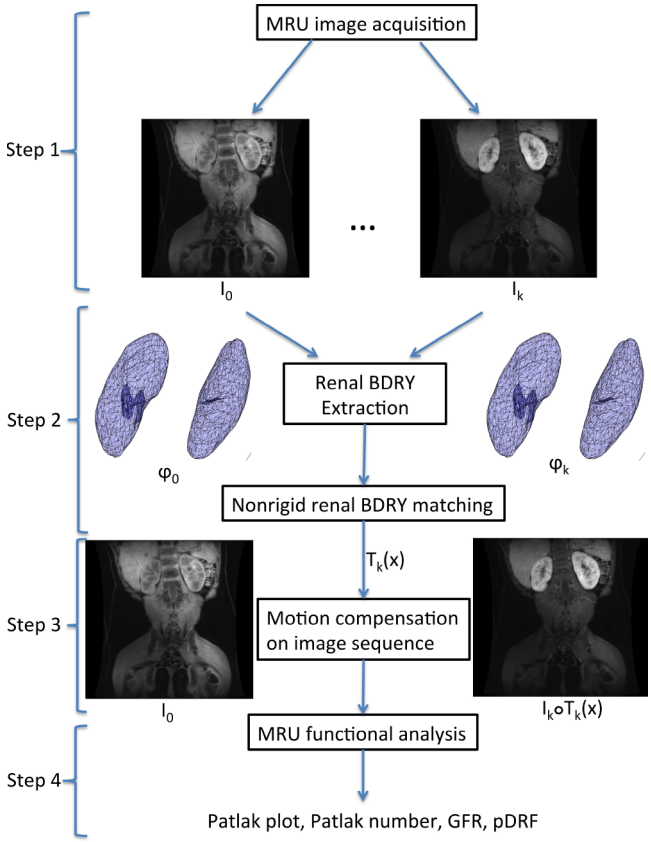

FIG. 4. Flowchart of the motion compensated MRU analysis: Step 1. MRU image acquisition (Sec. 2.A)—I_0 and I_k represent the acquired reference volume and image volumes at different time points, respectively; Step 2. Motion estimation with extracted renal boundaries (Sec. 2.C)—extracting renal boundaries of each image volume and estimating motion field at different time points $T_k(x)$ by registering ϕ_k with the reference ϕ_0; Step 3. Motion compensation on MRU image sequence—applying the obtained motion fields to each image volume $I_k(x) \circ T_k(x)$ and mapping the intensity at different times to a common spatial coordinate system (executed in MATLAB); Step 4. MRU functional analysis based on Sec. 2.B on the Osirix platform (Ref. 25).

2.B.3. pDRF

The pDRF is another potential GFR indicator that is slightly modified to incorporate a normalization of right vs left kidney Patlak numbers. It is calculated based on the following equations:

$$\text{pDRF}_R = \frac{P_R}{P_R + P_L}, \tag{4}$$

$$\text{pDRF}_L = \frac{P_L}{P_R + P_L}, \tag{5}$$

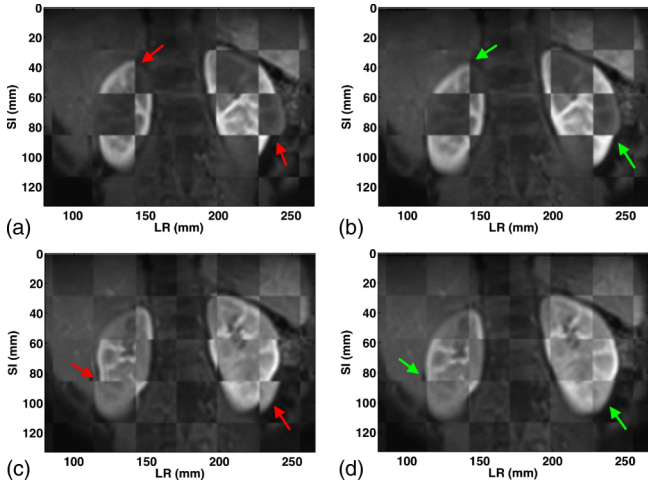

FIG. 5. Checkerboard visualization of registration results in different volumes from subject 1: (a) 22nd slice in volume 1 vs volume 11 before registration, (b) 22nd slice in volume 1 vs volume 11 after registration, (c) 22nd slice in volume 11 vs volume 17 before registration, and (d) 22nd slice in volume 11 vs volume 17 after registration; arrows in (a) and (b) indicate positions with misalignment and arrows in (c) and (d) indicate positions of improved continuity and alignment after motion compensation.

where P_L and P_R represent Patlak numbers calculated from the left and right kidneys, respectively. pDRF often serves as a more robust index than the Patlak number thanks to its normalization.[21,22]

2.C. Motion estimation in MRU

In this study, we propose to adopt our recent developed shape-based motion estimation method[12] for motion compensation in MRU analysis. Specifically, this algorithm consists of two sequential parts: (1) extracting renal boundary features with a level set based segmentation and (2) estimating nonrigid motion among extracted renal boundaries. Figure 3 illustrates the basic idea of the proposed motion correction scheme, which rids misleading perturbations caused by including the intensity of different voxels in the dynamic plot.

2.C.1. Extracting renal boundaries: Level set based segmentation

The level set method, first introduced by Osher and Fedkiw,[23] is a powerful tool representing evolving curves and surfaces and is widely used in various segmentation tasks. In the level set representation, a curve C is usually represented implicitly as the zero level set of its corresponding level set function (LSF) ϕ in a higher dimensional space. Here, we represent renal boundary features by the level set function ϕ and perform segmentation by minimizing a variational energy that encodes several priors,

$$\epsilon(\phi) = \lambda \mathcal{L}_g(\phi) + \frac{\beta}{2}\mathcal{A}(\phi) + \mu \mathcal{R}_p(\phi), \tag{6}$$

where $\mathcal{L}_g(\phi) = \int_\Omega g\delta(\phi)|\nabla\phi| d\mathbf{x}$ regularizes the curve length and smoothness, with g representing the edge indication function. Cross-frame consistency is encouraged with $\mathcal{A}(\phi) = ((\int_\Omega H(-\phi)d\mathbf{x}) - (\int_\Omega H(-\phi_0)d\mathbf{x}))^2$ by minimizing the l_2 distance of renal volumes between adjacent frames, with $\int_\Omega H(-\phi)d\mathbf{x}$ representing the target renal volume and $\int_\Omega H(-\phi_0)d\mathbf{x}$ representing the renal volume of the previous frame. Here, H is the Heaviside function. The signed distance property of the level set function is regularized by $\mathcal{R}_p(\phi) = \int_\Omega p(|\nabla\phi|)d\mathbf{x}$, where p is designed as a proper double-well function with minimal values at 0 and 1.[24] A gradient descent method has been derived and applied to minimize the above energy functional to obtain the proper shape segmentation. The initialization of the level set segmentation takes advantage of the temporal continuity of anatomical structures extracted from the images. The level set curve from segmenting a volume preceding in time is used to initialize the segmentation for a subsequence volume. The segmentation of the first volume is initialized manually.

2.C.2. Nonrigid motion estimation

After extracting renal boundaries of the volumetric image at each time, we match renal boundaries ϕ_i of different volumes with the reference ϕ_0,

$$E(\boldsymbol{\omega}) = \int_{\Omega_{nb}} (\phi_0(\mathbf{x}) - \phi_i(\mathbf{x}+\boldsymbol{\omega}))^2 d\mathbf{x} + \alpha \int_\Omega \|\nabla\boldsymbol{\omega}\|_F^2 d\mathbf{x}, \tag{7}$$

where $\boldsymbol{\omega}$ is the motion to estimate, ϕ_0 and ϕ_i represent extracted renal boundaries of the reference and target volumes, respectively, and α is the smoothness regularization coefficient. The fidelity is restricted over a narrowband region to be resilient to noise away from the renal boundaries: $\Omega_{nb} = \{\mathbf{x} : |\phi_1(\mathbf{x})| < \eta\} \cup \{\mathbf{x} : |\phi_2(\mathbf{x})| < \eta\}$, where 2η is the width of the detected renal boundaries centered at the zero level set. The above energy functional is minimized by solving the corresponding Euler–Lagrange equations through two nested iterative schemes. Algorithmic and numerical details are provided in Ref. 12. For all segmentation performed in this study, we manually fixed the smoothness length, area, signed distance parameters, and time step to be $\lambda = 0.5$, $\beta = 0.001$, $\mu = 0.2$, and $\Delta t = 1$, respectively. In all motion estimation performed, the smoothness weight α and the width of the narrowband η were set to 1.5 and 15 voxels, respectively, in all experiments. Without specific code optimization, the total computation time for both segmentation and motion estimation between two 3D volumes with size $256\times256\times34$ is about 2 min. It takes about 60 min for processing a whole sequence of DCE-MR images that usually contains about 30 time frames.

TABLE I. Error statistics of registration results on DCE-MR images, showing subvoxel accuracy (voxel size = $1.33 \times 1.33 \times 4$ mm).

	MAE	RMSE	SD	Mean	Median
Left–right (mm)	0.25	0.43	0.43	−0.02	−0.01
Superior–inferior (mm)	0.14	0.29	0.29	−0.04	−0.01
Anterior–posterior (mm)	0.30	0.46	0.46	0.01	0.01
3D (mm)	0.49	0.70	0.50	0.49	0.35

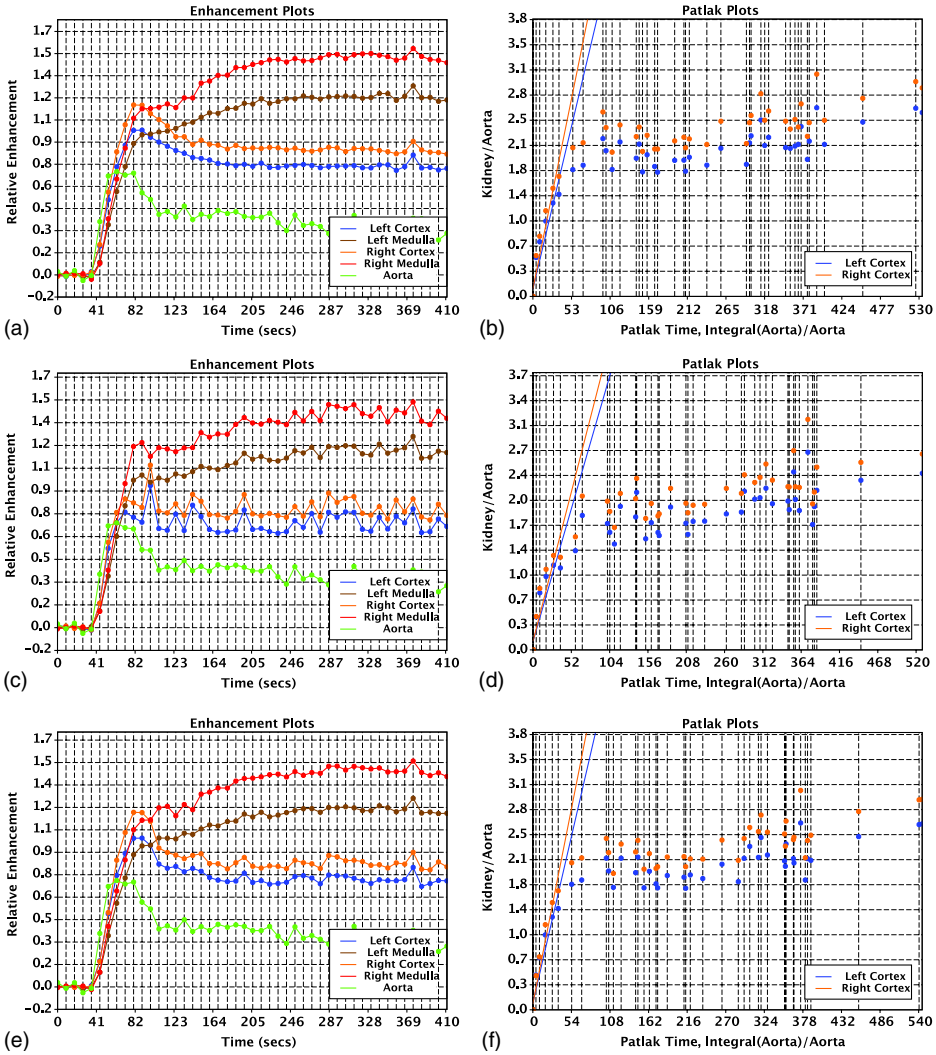

FIG. 6. Comparison of enhancement curves and Patlak plot from subject 1: (a) and (b) ground truth enhancement curves and Patlak plot, (c) and (d) enhancement curves and Patlak plots generated from unregistered datasets, (e) and (f) enhancement curves and Patlak plots after motion compensation.

2.D. Motion compensated MRU analysis

Figure 4 illustrates the proposed flowchart of incorporating the introduced motion correction method into the MRU analysis with four specific steps.

2.E. Experiments

To validate the proposed motion compensation scheme, we propose the following two sets of complementary experiments.

2.E.1. Experiment on sedated DCE-MR images with simulated motion for quantitative assessment

MRU analysis was first performed on the DCE-MR images acquired from three sedated children subjects that have significant variations in their anatomical structures and enhancement behaviors (Fig. 1), from which clinically valid functional estimates were calculated as the ground truth.

To mimic the realistic renal motion under respiration, we carefully synthesized a nonrigid motion field based on the well-accepted B-spline model,[26] which was flexible enough to characterize physical and physiological motion.[27] The simulated nonrigid field had predominant motions in the SI and left–right (LR) directions with average motion magnitude of 15 and 9 mm, respectively. To mimic the inconsistent renal positions of different breath-holds, the motion magnitude applied to each volume was multiplied with a random number between 0 and 1. The synthesized datasets were generated by applying the simulated motions to the original image volumes.

We quantitatively evaluated the impact of nonrigid motion on functional estimates and the efficacy of the introduced motion compensated MRU framework by comparing calculations without and with motion compensation against the ground truth for the following functional information: the relative enhancement curves, Patlak number, GFR, and pDRF.

2.E.2. Experiment on free-breathing MR images

We applied the proposed method to the noncontrast free-breathing MR images (Fig. 2). The performance on compensating real motion was evaluated by comparing the standard

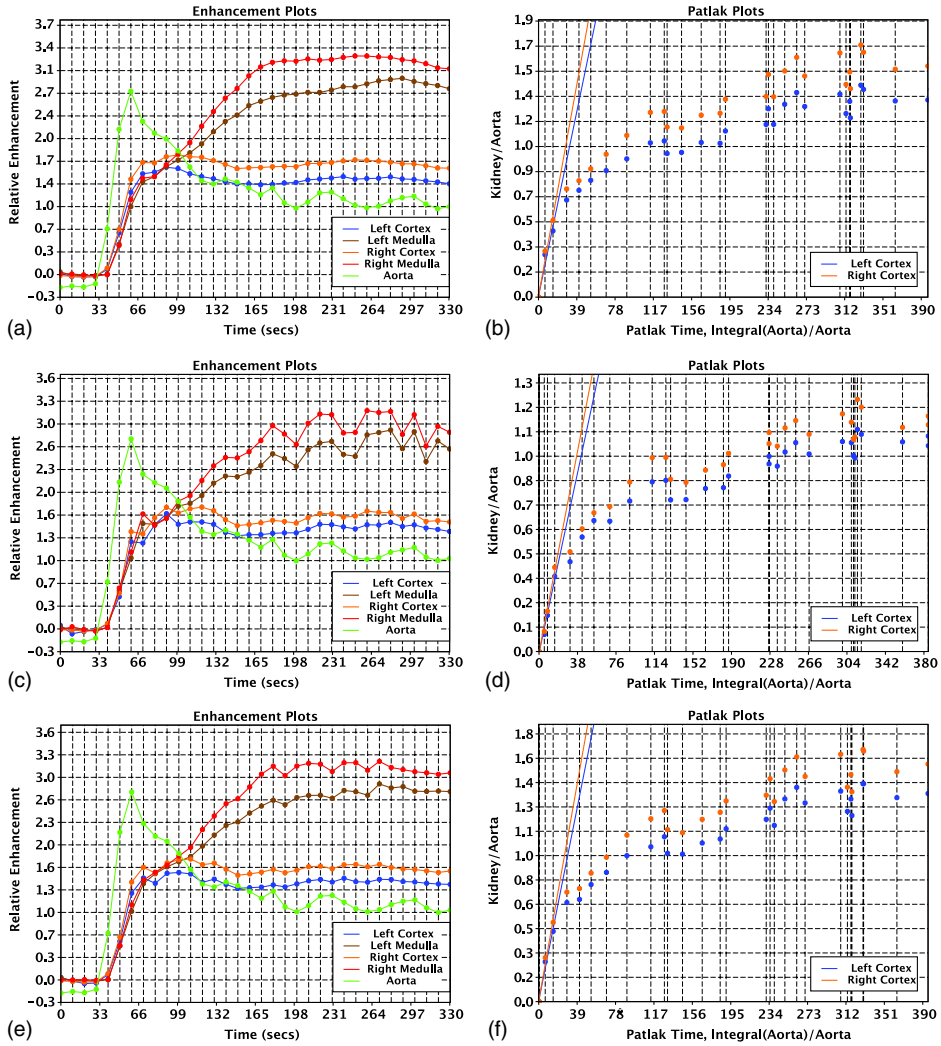

FIG. 7. Comparison of enhancement curves and Patlak plot from subject 2: (a) and (b) ground truth enhancement curves and Patlak plot, (c) and (d) enhancement curves and Patlak plots generated from unregistered datasets, (e) and (f) enhancement curves and Patlak plots after motion compensation.

deviation of the temporal intensity curves before and after motion compensation for two selected ROIs.

3. RESULTS

3.A. Motion correction results on sedated DCE-MR images with simulated motion

Figure 5 provides the checkerboard representations of example slices in different volumes before and after motion correction, where pronounced improvement on the boundary continuities can be observed after registration. We denote $e_i(\mathbf{x}) = \omega_i(\mathbf{x}) - \hat{\omega}_i(\mathbf{x})$ as the error in each direction by calculating the difference between the ground truth and the estimated motion for voxels $\mathbf{x}$ within proper neighborhood of the kidneys and $e(\mathbf{x}) = \sqrt{\sum_{i=1}^{3}(\omega_i(\mathbf{x}) - \hat{\omega}_i(\mathbf{x}))^2}$ as the aggregated error. We report mean absolute error ($\mathrm{MAE} = 1/N \sum_{i=1}^{N} |e_i|$), root mean squared error ($\mathrm{RMSE} = \sqrt{1/N \sum_{i=1}^{N} e_i^2}$), standard deviation (SD), mean, and median of e_i in Table I.

3.B. Quantitative MRU analysis results

The quantitative functional information obtained from our analysis were compared with the ground truth. The first five volumes for each subject were chosen as the precontrast baseline scans to compensate for the low SNR.

The relative enhancement curves and Patlak plots generated from unregistered and registered datasets were compared in Figs. 6–8 for each subject, respectively. The enhancement curves exhibited much less perturbations after motion compensation for all three subjects. Moreover, the corticomedullary crossover points, which were quite inconspicuous from nonregistered datasets, became clearly visible and close to the ones in true enhancement plots after registration. The Patlak number, pDRF, and GFR from each subject were calculated and compared with the ground truth. As shown in Table II, the estimated Patlak numbers from unregistered datasets were significantly underestimated up to 35% and 34% for the left and right kidneys, respectively. After motion compensation, the Patlak number estimation errors for the left and right kidneys were reduced within 4% and 3%,

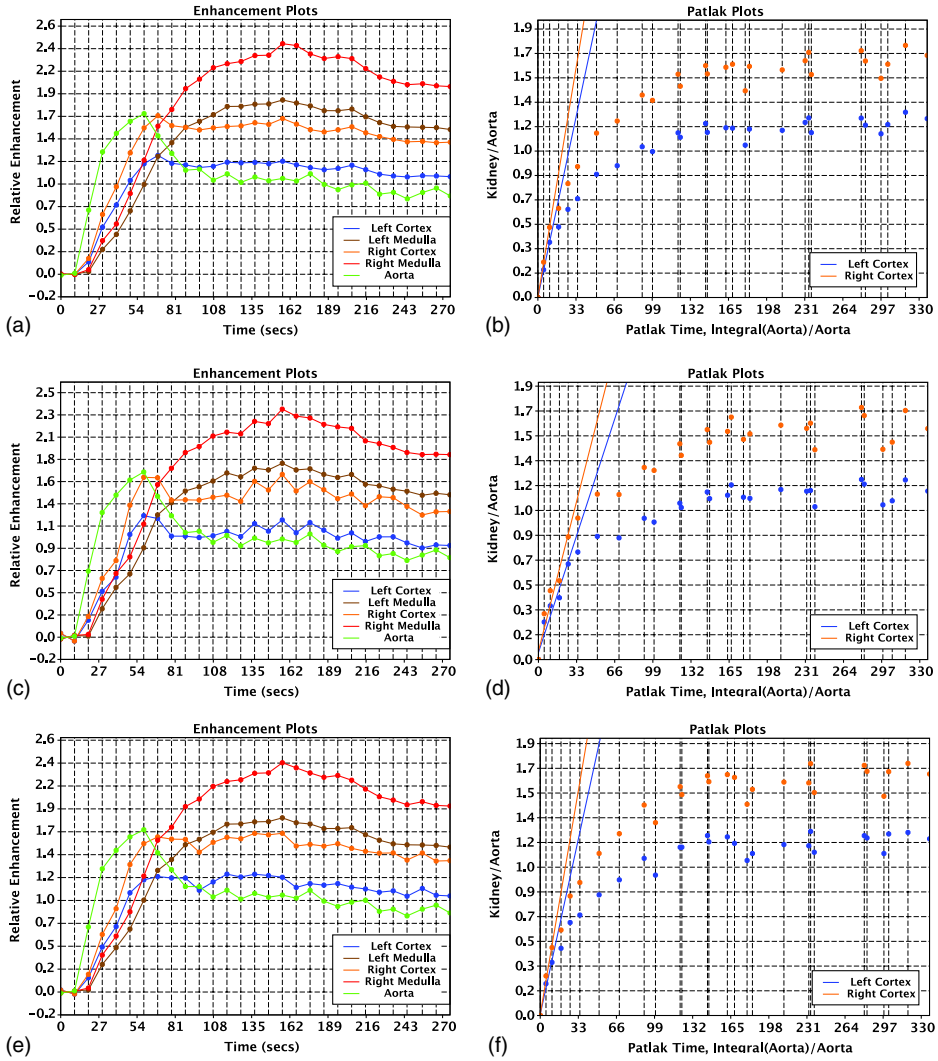

FIG. 8. Comparison of enhancement curves and Patlak plot from subject 3: (a) and (b) ground truth enhancement curves and Patlak plot, (c) and (d) enhancement curves and Patlak plots generated from unregistered datasets, (e) and (f) enhancement curves and Patlak plots after motion compensation.

respectively, demonstrating the efficacy of the proposed MRU motion compensation framework.

3.C. Motion compensation results on free-breathing MR images

Figure 9 compares the temporal intensity curves before and after motion correction within two manually selected ROIs. In the ideal scenario without contrast injection/motion, one expects the intensity curve to be stable and close to constant over the time course. The presence of free-breathing motion severely perturbed the intensity curve, introducing potential misleading effects in the subsequent analysis if any. After motion correction, the intensity curve became more stable/constant, coinciding with the expected behavior, and the standard deviation decreased from 30.3 and 38.2 to 8.3 and 11.7 for the two selected ROIs, respectively. Figure 10 provides the checkerboard representations of example slices in different volumes before and after motion correction, where pronounced improvement of alignment can be observed.

4. DISCUSSION

The presence of nonrigid motion on DCE-MR dataset introduced large artificial perturbations in the observed temporal trajectory of voxel intensity and led to large deviations in the subsequent functional estimates. The proposed motion compensation scheme provided pronounced improvement in correcting motion and generating more faithful enhancement curve presentations: better quantitative assessment of Patlak estimation demonstrated the end-to-end performance gain, and the reduced temporal variations in noncontrast free-breathing MR tests were suggestive of good performance in the presence of real motion.

Some residual perturbations in the relative enhancement curves persisted after motion correction. One may attribute this residual to the fact that geometric contour matching may not be fully capable of recovering voxelwise correspondence, especially in the far interior/exterior of the anatomical structures. However, such small misregistrations had little impact on the estimated Patlak numbers.

TABLE II. Comparison of estimated functional parameters for each subject: the ground truth values were calculated from the original DCE-MR images with subjects under sedation.

		Ground truth		Unregistered		Registered	
		Left kidney	Right kidney	Left kidney	Right kidney	Left kidney	Right kidney
Subject 1	Patlak (ml/min/ml)	2.6	3.0	2.1	2.3	2.6	3.0
	GFR (ml/min)	101.9	134.3	83.0	105.3	103.0	135.9
	pDRF (%)	46.1	53.9	47.1	52.9	46.1	53.9
Subject 2	Patlak (ml/min/ml)	1.9	2.2	1.4	1.6	1.9	2.2
	GFR (ml/min)	80.7	115.1	58.6	81.7	81.9	114.6
	pDRF (%)	46.6	53.4	47.2	52.8	47.1	52.9
Subject 3	Patlak (ml/min/ml)	2.3	2.9	1.5	1.9	2.2	2.8
	GFR (ml/min)	67.9	88.2	43.3	56.7	65.2	85.1
	pDRF (%)	44.0	56.0	43.8	56.2	43.9	56.1

In this study, the Patlak number was estimated from the two-compartment Patlak–Rutland model and GFR was calculated as the product of the absolute Patlak number with the renal volume. This simplified model has shown good agreement with GFR values obtained using a reference method.[28,29] Further improvement can be achieved by correcting for the hematocrit and accounting for the patient's weight.[21,30] The value derived from the slope of the Rutland–Patlak plot is more desirable to be treated as a GFR index instead of an absolute measurement. More extensive validations are needed especially in children.[21,22]

In our experiments, though the Patlak numbers were underestimated from the unregistered datasets from different subjects, the calculated pDRF was quite robust to the motion artifacts. This agrees with the general observation that the pDRF is more robust to the imperfection of input signals and can serve as a relatively robust measurement of renal function in children.[21,22]

Compared with other motion correction approaches based on either mutual information or cross-correlation metric,[8,9] the proposed shape-based registration scheme is more robust to local intensity changes across frames as in DCE-MR images and yields more accurate motion correction results.[12] With the advantage of its robustness to contrast and intensity variations, the proposed shape-based motion compensation scheme, upon further validation, has the potential to be applicable to other quantitative DCE analysis, such as functional liver or prostate analysis.[31,32]

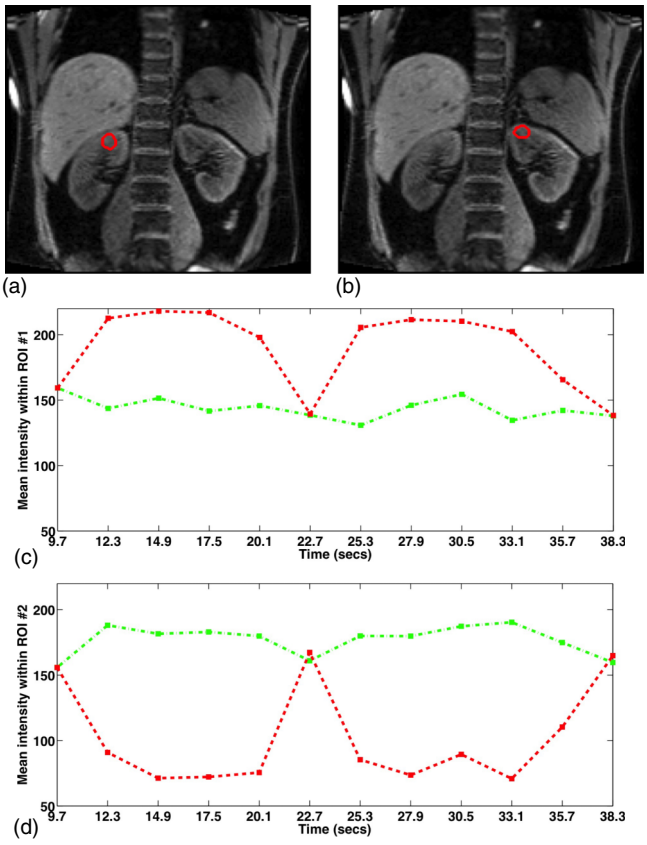

FIG. 9. Comparison of temporal intensity curves within two selected ROIs before and after motion compensation: (a) selected ROI 1, (b) selected ROI 2, (c) comparison of temporal intensity curves for ROI 1, and (d) comparison of temporal intensity curves for ROI 2. Red dashed lines represent temporal intensity curves before motion correction and green dashed–dotted lines indicate temporal intensity curves after motion correction.

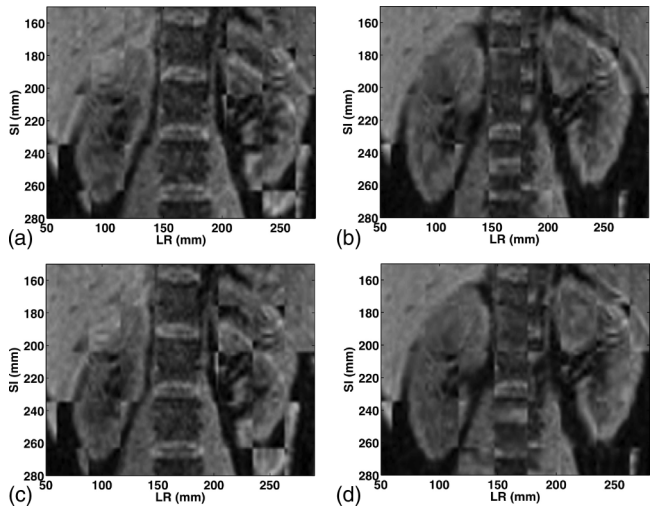

FIG. 10. Checkerboard visualization of registration results in different volumes from noncontrast free-breathing MR dataset: (a) 14th slice in volume 1 vs volume 5 before registration, (b) 14th slice in volume 1 vs volume 5 after registration, (c) 14th slice in volume 1 vs volume 10 before registration, and (d) 14th slice in volume 1 vs volume 10 after registration.

Besides the utility in pediatric MRU to alleviate the burden of sedation for children, the proposed technique also has a direct application to adult DCE-MRI in compensating motion between multiple short breath-holds and reducing the sacrifice in scanning efficiency from gating.

5. CONCLUSION

We have shown that our proposed MRU motion correction framework has good promise in compensating motion artifacts to facilitate functional MRU analysis. On DCE-MR dataset with simulated motion, the Patlak estimation errors have been significantly reduced from 35% and 34% to 4% and 3% for the left and right kidneys, respectively. On free-breathing MR dataset without contrast, the proposed method has achieved significantly reduced standard deviation of the temporal intensity curves. Future work includes (a) performing more intensive clinical verifications with sophisticated pharmacokinetic models, (b) pursuing an institutional review board approved protocol to acquire free-breathing DCE-MRI measurement, and (c) generalizing the proposed method to other quantitative DCE analysis, such as on liver or prostate function.

[a]Author to whom correspondence should be addressed. Electronic mail: druan@mednet.ucla.edu

[1]C. Hayes, A. R. Padhani, and M. O. Leach, "Assessing changes in tumor vascular function using dynamic contrast-enhanced magnetic resonance imaging," NMR Biomed. **15**(2), 154–163 (2002).
[2]E. F. Avni, M. A. Bali, M. Regnault, N. Damry, F. Degroot, T. Metens, and C. Matos, "MR urography in children," Eur. J. Radiol. **43**(2), 154–166 (2002).
[3]J. D. Grattan-Smith and R. A. Jones, "MR urography in children," Pediatr. Radiol. **36**(11), 1119–1132 (2006).
[4]B. R. Huch, J. Debatin, and G. Krestin, "Contrast-enhanced MR imaging of the kidneys and adrenal glands," Magn. Reson. Imaging Clin. North Am. **4**(1), 101–131 (1996).
[5]A. Melbourne, J. Hipwell, M. Modat, T. Mertzanidou, H. Huisman, S. Ourselin, and D. Hawkes, "The effect of motion correction on pharmacokinetic parameter estimation in dynamic-contrast-enhanced MRI," Phys. Med. Biol. **56**(24), 7693–7708 (2011).
[6]J. Tokuda, H. Mamata, R. R. Gill, N. Hata, R. Kikinis, R. F. Padera, R. E. Lenkinski, D. J. Sugarbaker, and H. Hatabu, "Impact of nonrigid motion correction technique on pixel-wise pharmacokinetic analysis of free-breathing pulmonary dynamic contrast-enhanced MR imaging," J. Magn. Reson. Imaging **33**(4), 968–973 (2011).
[7]V. S. Lee, H. Rusinek, M. E. Noz, P. Lee, M. Raghavan, and E. L. Kramer, "Dynamic three-dimensional MR renography for the measurement of single kidney function: Initial experience," Radiology **227**(1), 289–294 (2003).
[8]A. D. Merrem, F. G. Zöllner, M. Reich, A. Lundervold, J. Rorvik, and L. R. Schad, "A variational approach to image registration in dynamic contrast-enhanced MRI of the human kidney," Magn. Reson. Imaging **31**(5), 771–777 (2013).
[9]F. G. Zöllner, R. Sance, P. Rogelj, M. J. Ledesma-Carbayo, J. Rørvik, A. Santos, and A. Lundervold, "Assessment of 3D DCE-MRI of the kidneys using non-rigid image registration and segmentation of voxel time courses," Comput. Med. Imag. Grap. **33**(3), 171–181 (2009).
[10]G. P. Penney *et al.*, "A comparison of similarity measures for use in 2-D–3-D medical image registration," IEEE. Trans. Med. Imaging **17**(4), 586–595 (1998).
[11]J. P. Pluim, J. A. Maintz, and M. A. Viergever, "Image registration by maximization of combined mutual information and gradient information," in *Medical Image Computing and Computer-Assisted Intervention–MICCAI 2000* (Springer, Berlin, 2000), pp. 452–461.
[12]W. Liu and D. Ruan, "Estimating nonrigid motion from inconsistent intensity with robust shape features," Med. Phys. **40**, 121912 (13pp.) (2013).
[13]M. Saranathan, D. W. Rettmann, B. A. Hargreaves, S. E. Clarke, and S. S. Vasanawala, "Differential subsampling with cartesian ordering (DISCO): A high spatio-temporal resolution dixon imaging sequence for multiphasic contrast enhanced abdominal imaging," J. Magn. Reson. Imaging **35**(6), 1484–1492 (2012).
[14]Y. Le, R. Kroeker, H. D. Kipfer, and C. Lin, "Development and evaluation of TWIST Dixon for dynamic contrast-enhanced (DCE) MRI with improved acquisition efficiency and fat suppression," J. Magn. Reson. Imaging **36**(2), 483–491 (2012).
[15]R. A. Jones, K. Easley, S. B. Little, H. Scherz, A. J. Kirsch, and J. D. Grattan-Smith, "Dynamic contrast-enhanced MR urography in the evaluation of pediatric hydronephrosis: Part 1, functional assessment," Am. J. Rhinol. **185**(6), 1598–1607 (2005).
[16]H. S. Teh, E. S. Ang, W. C. Wong, S. B. Tan, A. G. S. Tan, S. M. Chng, M. B. K. Lin, and J. S. K. Goh, "MR renography using a dynamic gradient-echo sequence and low-dose gadopentetate dimeglumine as an alternative to radionuclide renography," Am. J. Roentgenol. **181**(2), 441–450 (2003).
[17]B. B. McDaniel, R. A. Jones, H. Scherz, A. J. Kirsch, S. B. Little, and J. D. Grattan-Smith, "Dynamic contrast-enhanced MR urography in the evaluation of pediatric hydronephrosis: Part 2, anatomic and functional assessment of uteropelvic junction obstruction," Am. J. Roentgenol. **185**(6), 1608–1614 (2005).
[18]C. S. Patlak *et al.*, "Graphical evaluation of blood-to-brain transfer constants from multiple-time uptake data," J. Cereb. Blood Flow Metab. **3**(1), 1–7 (1983).
[19]A. Peters, "Graphical analysis of dynamic data: The Patlak-Rutland plot," Nucl. Med. Commun. **15**(9), 669–672 (1994).
[20]M. Rutland, "A single injection technique for subtraction of blood background in 131i-hippuran renograms," Br. J. Radiol. **52**(614), 134–137 (1979).
[21]R. A. Jones, B. Schmotzer, S. B. Little, and J. D. Grattan-Smith, "MRU post-processing," Pediatr. Radiol. **38**(1), 18–27 (2008).
[22]I. Mendichovszky, M. Pedersen, J. Frøkiær, T. Dissing, N. Grenier, P. Anderson, K. McHugh, Q. Yang, and I. Gordon, "How accurate is dynamic contrast-enhanced MRI in the assessment of renal glomerular filtration rate? A critical appraisal," J. Magn. Reson. Imaging **27**(4), 925–931 (2008).
[23]S. Osher and R. Fedkiw, *Level Set Methods and Dynamic Implicit Surfaces* (Springer, New York, NY, 2003), Vol. 153.
[24]C. Li, C. Xu, C. Gui, and M. D. Fox, "Distance regularized level set evolution and its application to image segmentation," IEEE. Trans. Image Process. **19**(12), 3243–3254 (2010).
[25]A. Rosset and L. Spadola, "Osirix: An open-source software for navigating in multidimensional DICOM images," J. Digit. Imaging **17**(3), 205–216 (2004).
[26]M. Unser, A. Aldroubi, and M. Eden, "Fast B-spline transforms for continuous image representation and interpolation," IEEE Trans. Pattern Anal. Mach. Intell. **13**(3), 277–285 (1991).
[27]W. P. Segars, D. S. Lalush, and B. M. Tsui, "Modeling respiratory mechanics in the MCAT and spline-based MCAT phantoms," IEEE. Trans. Nucl. Sci. **48**(1), 89–97 (2001).
[28]D. L. Buckley, A. E. Shurrab, C. M. Cheung, A. P. Jones, H. Mamtora, and P. A. Kalra, "Measurement of single kidney function using dynamic contrast-enhanced MRI: Comparison of two models in human subjects," J. Magn. Reson. Imaging **24**(5), 1117–1123 (2006).
[29]N. Hackstein, J. Heckrodt, and W. S. Rau, "Measurement of single-kidney glomerular filtration rate using a contrast-enhanced dynamic gradient-echo sequence and the Rutland-Patlak plot technique," J. Magn. Reson. Imaging **18**(6), 714–725 (2003).
[30]I. Sharkey, A. Boddy, H. Wallace, J. Mycroft, R. Hollis, and S. Picton, "Body surface area estimation in children using weight alone: Application in pediatric oncology," Br. J. Cancer **85**(1), 23 (2001).
[31]Y. Cao, J. Alspaugh, Z. Shen, J. M. Balter, T. S. Lawrence, and R. K. Ten Haken, "A practical approach for quantitative estimates of voxel-by-voxel liver perfusion using DCE imaging and a compartmental model," Med. Phys. **33**(8), 3057–3062 (2006).
[32]S. Viswanath, B. N. Bloch, M. Rosen, J. Chappelow, R. Toth, N. Rofsky, R. Lenkinski, E. Genega, A. Kalyanpur, and A. Madabhushi, "Integrating structural and functional imaging for computer assisted detection of prostate cancer on multi-protocol in vivo 3 Tesla MRI," Proc. SPIE **7260**, 72603I (2009).